GFZ
Helmholtz-Zentrum
POTSDAM

Originally published as:

Lopez Comino, J. A., Cesca, S., Kriegerowski, M., Heimann, S., Dahm, T., Mirek, J., Lasocki, S. (2017): Monitoring performance using synthetic data for induced microseismicity by hydrofracking at the Wysin site (Poland). - *Geophysical Journal International*, *210*, 1, pp. 42—55.

DOI: http://doi.org/10.1093/gji/ggx148

Geophysical Journal International

Geophys. J. Int. (2017) **210,** 42–55
Advance Access publication 2017 April 17
GJI Seismology

doi: 10.1093/gji/ggx148

Monitoring performance using synthetic data for induced microseismicity by hydrofracking at the Wysin site (Poland)

J.A. López-Comino,[1] S. Cesca,[1] M. Kriegerowski,[1,2] S. Heimann,[1] T. Dahm,[1] J. Mirek[3] and S. Lasocki[3]

[1]*GFZ German Research Centre for Geosciences, Telegrafenberg, D-*14473 *Potsdam, Germany. E-mail: jalopez@gfz-potsdam.de*
[2]*Institute of Earth and Environmental Sciences, University of Potsdam, D-*14476 *Potsdam-Golm, Germany*
[3]*Institute of Geophysics, Polish Academy of Sciences, ul. Ksiecia Janusza* 64, *PL-*01-452 *Warsaw, Poland*

Accepted 2017 April 11. Received 2017 April 7; in original form 2017 January 30

SUMMARY

Ideally, the performance of a dedicated seismic monitoring installation should be assessed prior to the observation of target seismicity. This work is focused on a hydrofracking experiment monitored at Wysin, NE Poland. A microseismic synthetic catalogue is generated to assess the monitoring performance during the pre-operational phase, where seismic information only concerns the noise conditions and the potential background seismicity. Full waveform, accounting for the expected spatial, magnitude and focal mechanism distributions and a realistic local crustal model, are combined with real noise recording to produce either event based or continuous synthetic waveforms. The network detection performance is assessed in terms of the magnitude of completeness (M_c) through two different techniques. First, we use an amplitude threshold, taking into the ratio among the maximal amplitude of synthetic waveforms and station-dependent noise levels, for different values of signal-to-noise ratio. The detection probability at each station is estimated for the whole data set and extrapolated to a broader range of magnitude and distances. We estimate an M_c of about 0.55, when considering the distributed network, and can further decrease M_c to 0.45 using arrays techniques. The second approach, taking advantage on an automatic, coherence-based detection algorithm, can lower M_c to ~ 0.1, at the cost of an increase of false detections. M_c experiences significant changes during day hours, in consequence of strongly varying noise conditions. Moreover, due to the radiation patterns and network geometry, double-couple like sources are better detected than tensile cracks, which may be induced during fracking.

Key words: Earthquake interaction, forecasting, and prediction; Earthquake monitoring and test-ban treaty verification; Induced seismicity.

1 INTRODUCTION

Induced seismicity related to industrial processes including shale gas and oil exploitation, mining and other energy technologies are current issues that imply enough reasons to be concerned (Nicholson & Wesson 1990, 1992; McGarr *et al*. 2002; Davies *et al*. 2013; Ellsworth 2013). The assessment of the potential hazard for these triggered or induced earthquakes has become a relevant and pressing problem, especially because seismicity rates have increased in some locations. In the Western Canada Sedimentary Basin, seismic activity has been conjectured as being induced by hydraulic fracturing (Farahbod *et al*. 2015; Schultz *et al*. 2015a), gas extraction (Baranova *et al*. 1999) or waste water disposal (Horner *et al*. 1994; Schultz *et al*. 2014). Fracking operations in the United Kingdom were stopped for several years after the detection of two earthquakes with magnitudes of M_L 2.3 and 1.5 in the Blackpool area (Clarke *et al*. 2014). An interesting case correlated to gas injection operations occurred offshore Spain, in the Gulf of Valencia, recording a maximum moment magnitude M_w 4.3 on 2013 October 1 (Cesca *et al*. 2014; Gaite *et al*. 2016). The major cause of injection-induced earthquakes is associated with the disposal of wastewater into deep strata (Healy *et al*. 1968) and the largest events in that respect were registered in Oklahoma in 2011 November, reaching a peak magnitude of M_w 5.7 (Keranen *et al*. 2013). Other instances of induced seismicity, sometimes including events of $M > 4$, have been observed in recent years (Ellsworth 2013; Holland 2013). This work focuses on recent hydraulic fracturing operations associated to shale gas exploration and exploitation in Poland, due to the increased interest in these techniques in some European countries (SHEER project, www.sheerproject.eu).

Hydraulic fracturing usually induces weak events since the volumes of injected fluids are small (Davies *et al*. 2013). However, scenarios with larger earthquakes are possible, for example, if the injected fluids alter friction conditions and trigger the failure of

© The Authors 2017. Published by Oxford University Press on behalf of The Royal Astronomical Society.

neighbouring faults under pre-existing, tectonic stress. For example, at the Horn River Basin, British Columbia, a sequence of earthquakes reaching M_w 3 was caused by fluid injection in proximity of pre-existing faults (British Columbia Oil and Gas Commission 2012). Hydrofracking occurs when the pore pressure exceeds the minimal principal stress and the local strength is overcome. As a result of fracking, microearthquakes and aseismic slip creates the pathways for the gas/oil, enhancing the rock permeability. In general, the crack growth stops when the rupture runs out of energy. However, the progressing crack could find new energy sources, for example, in presence of tectonically loaded faults. Seismic monitoring of fracking operations is essential, so that branching out of seismicity is early detected and correlated with geomechanical operations. The ability of a local network to detect weak microearthquakes as well as larger triggered events depends on the seismic instrumentation, station number, network geometry, seismic noise and installation conditions. Consequently, assessing the performance of the monitoring setup, for example, estimating the expected magnitude of completeness (M_c) or the smallest detectable magnitude, is a fundamental step for a later reliable analysis of the forthcoming seismicity. In this work, we discuss how to address the problem of detection performance before the target hydraulic fracturing operation takes place. With this goal, we make use of the concept of M_c, defined as the lowest magnitude at which 100 per cent of the earthquakes in a space–time volume are reliably detected (e.g. Rydelek & Sacks 1989; Wiemer & Wyss 2000; Woessner & Wiemer 2005).

Multiple techniques have been proposed for the estimation of M_c. Mignan & Woessner (2012) classify them as catalogue-based and network-based methods. The first group of methodologies is mostly based on the assumption of self-similarity of the earthquake process, implying that M_c is the minimum magnitude at which the observed cumulative frequency magnitude distribution departs from the Gutenberg–Richter law (Wiemer & Wyss 2000; Cao & Gao 2002; Marsan 2003; Woessner & Wiemer 2005; Amorese 2007; Mignan *et al*. 2011). The second category uses the network distribution to estimate M_c: this is either done through the analysis of diurnal variations (Rydelek & Sacks 1989), the comparison of amplitude–distance curves and the signal-to-noise ratio (SNR, Sereno & Bratt 1989), seismic threshold monitoring (Gomberg 1991; Kværna & Ringdahl 1999; Kværna *et al*. 2002), numerical simulation (D'Alessandro *et al*. 2011a,b; D'Alessandro & Stickney 2012), Bayesian statistics (Mignan *et al*. 2011; Kraft *et al*. 2013; Mignan & Chouliaras 2014) and detection probability estimates for each seismic station (Schorlemmer & Woessner 2008; Nanjo *et al*. 2010; Plenkers *et al*. 2011; Maghsoudi *et al.* 2013, 2015). Furthermore, understanding the microseismic source mechanisms and stress state has gained more interest recently and should be considered in an appropriate estimation of the detection performance (Nolen-Hoeksema & Ruff 2001; Baig & Urbancic 2010).

All the catalogue-based methods described above can only be used in a retroprospective manner, typically after several years of monitoring under the assumption of a steady earthquake generation process. This is not useful for planning the monitoring of fracking operations, which last only few months and are highly transient processes. Therefore, we propose a prospective evaluation method where we apply a combination of the aforementioned methods and synthetic data in order to assess the monitoring performance before the fracking operations start. To achieve this goal, we discuss how to generate a realistic synthetic microseismic catalogue and synthetic waveform data sets, accounting for the main characteristics of the expected source mechanisms for hydraulic fracturing as well as realistic noise conditions. The detection performance is assessed for the synthetic data using two different techniques. In the first case, we use an amplitude threshold, taking into account a station-dependent noise level and different values of SNR. In this case, the detection probability of each station is estimated for each synthetic event, and extrapolated to a broader range of magnitudes and distances from Bayesian statistics. The final map of the M_c is then estimated by combining the detection performance of different stations, considering the network geometry. The second approach follows the application of an automatic detection algorithm to the continuous synthetic data set, comprised of synthetic event waveforms and continuous real noise data. In this study, we apply a recently developed automated full waveform detection algorithm based on the stacking of smooth characteristic function and the identification of high coherence in the signals recorded at different stations (Lassie, https://gitext.gfz-potsdam.de/heimann/lassie, Matos *et al*. 2016; Heimann *et al*., in preparation).

2 MONITORING NETWORK AT THE WYSIN SITE (POLAND)

In order to assess the sensitivity of microseismicity to hydraulic fracturing operations, we perform a seismic monitoring at a shale gas exploration/exploitation site in Pomerania (Poland). In this area, close to the village of Wysin, Polish Oil and Gas Company (PGNiG) drilled two horizontal boreholes, named Wysin 2H and Wysin 3H, designed for fracturing under Stara Kiszewa Concession No. 1/2011//p for prospecting and exploration of oil and natural gas. The horizontal boreholes are located at 3955 and 3865 m below the surface and they are oriented WNW-ESE with an approximate horizontal length of 1.7 km each.

The seismic monitoring installation is part of a broader survey concept, also monitoring groundwater conditions and air pollution, planned and deployed thanks to the EU project SHEER (www.sheerproject.eu). The network is composed of a surface installation and a shallow borehole installation, covering a region of 60 km^2 (Fig. 1). The surface network includes six broad-band stations surrounding the drilling site at distances of 2.1–4.3 km, with a good azimuthal coverage (maximal gap 90°). In addition, short-period stations are arranged in three small-scale arrays, with apertures between 450 and 950 m. Broad-band stations are equipped with GÜRALP CMG-3ESP sensors, and record continuously with a sampling rate of 200 Hz. Short-period stations are either equipped with a combination of MARK L-4C-3D sensors or GeoSIG VE-53-BB sensors. The sampling rate of all short-period stations is 500 Hz. The shallow underground installation is composed of three seismometers (Geotech Instruments KS-2000) installed at 50 m depth. The installation was started on summer 2015 and the network is fully operational since 2015 November. However, two borehole stations (GW3S and GW4S) had suffered from technical problems and were replaced by two other stations with sensors Nanometrics Trillium Compact Posthole 120 s at the end of 2016 April. For this reason, we exclusively use seismic data of 2016 May to characterize the noise level at each station. This period precedes the beginning of the hydrofracking operations, which started in 2016 June at a depth of about 4000 m.

3 SYNTHETIC MICROSEISMIC CATALOGUE

We adopt a recently developed tool to generate a synthetic catalogue and waveform data sets, which realistically accounts for the

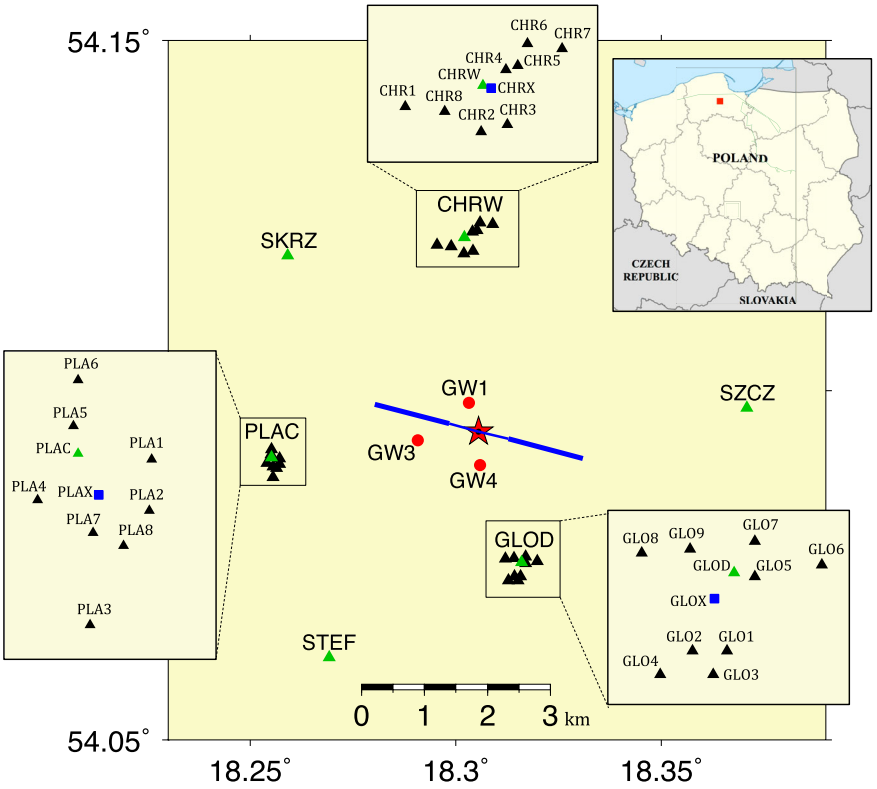

Figure 1. Map of seismic monitoring composed of six broad-band stations (green triangles), three small-scale arrays (inset boxes), each one composed of 8–9 short-period stations (black triangles) and three shallow borehole stations (red circles). Blue squares in inset boxes correspond to central locations of each array. Fracking area (red star, vertical borehole) and horizontal boreholes (blue lines) are shown. The inset map shows the fracking area (red square) in Poland.

expected microseismicity patterns (Kriegerowski *et al*. 2015). The procedure consists of two steps: (1) the generation of a synthetic seismic catalogue which reflects the characteristics of the expected seismic activity and, (2) based on that the generation of realistic synthetic full waveforms combined with real noise. We consider two types of seismicity in the study region: (i) a background seismicity, taking place independent from the fracking operations, with focal mechanisms controlled by the known orientation of tectonic stress and the unknown orientation of local faults, and (ii) induced seismicity, which is controlled in its growth and moment tensors by the superposition of tectonic and induced stresses. For this second group of potential microseismic events, the regional tectonic *in situ* stress state controls the direction of hydraulic fracture growth in the unperturbed rock formation (e.g. Nolen-Hoeksema & Ruff 2001; Zang & Stephansson 2010). The knowledge about the orientation of the maximum horizontal compressive stress (S_{Hmax}) is thus vital to establish possible candidate geometries for the expected focal mechanisms. The horizontal fracking drillings are expected to be perpendicular to S_{Hmax}, as such stress conditions favour the propagation of fractures opening in the direction of the least compressive stress (S_{h}). It has been shown that the processes involving rapid fluid injection can produce tensile failures with significant non-double-couple (DC) components, opening in the direction of the minimal compressive stress and closing after the injection (e.g. Economides & Nolte 2003 and others). The orientation of microfractures produced by the hydrofracking depends on the superposition of the stress perturbation induced by the hydraulic fracturing process and the background regional stress field.

Our synthetic catalogue should be consistent with the aforementioned conditions. For this purpose, we consider four families of microseismicity, assigning 1000 events to each one (Fig. 2); the subjective choice of the number of events has no major implications, since they are only used to assess the detection performance for different magnitudes and rupture types. We use a Hudson source-type plot (Hudson *et al*. 1989) to discuss the non-DC components and a graphical representation of tension (*T*), pressure (*P*) and null (*B*) axis to discuss the focal mechanism orientations. The first group of seismic sources (family 1) resembles the background seismicity: these sources are modeled by DC focal mechanisms (this group of synthetic events is hereafter referred as 'DC' family). Since the orientation of small local faults is unknown, we adopt a random distribution of orientations (i.e. random strikes and dips). The rake value, instead, is controlled by the strike and dip of the rupture plane and S_{Hmax} of the background stress. In our study area, located within the East European Craton geodynamic domains, the maximum horizontal stress is oriented $S_{\mathrm{Hmax}} \sim 15^{\circ}$ (World Stress Map database release 2008; Heidbach *et al*. 2008), almost perpendicular to the horizontal fracking drillings. The compressive regime implies the occurrence of thrust or strike-slip events, with no normal faulting (see triangular diagram in Fig. 2). To simulate possible minor deviations from a pure DC source due to the fluid injection, we include a random 10 per cent perturbation in the moment tensor entries. According to Baig & Urbancic (2010), induced fractures tend to open in the direction of the minimal compressive stress, closing in the same direction after the injection. We thus model two families of moment tensors, dominated by positive (family 2) and negative (family 3) tensile cracks with dipoles oriented parallel to S_{h} with a randomized deviations of $\pm 25^{\circ}$ (according the quality data for this orientation from the World Stress Map); also in this case, moment tensor configurations are finally perturbed, as for the DC family.

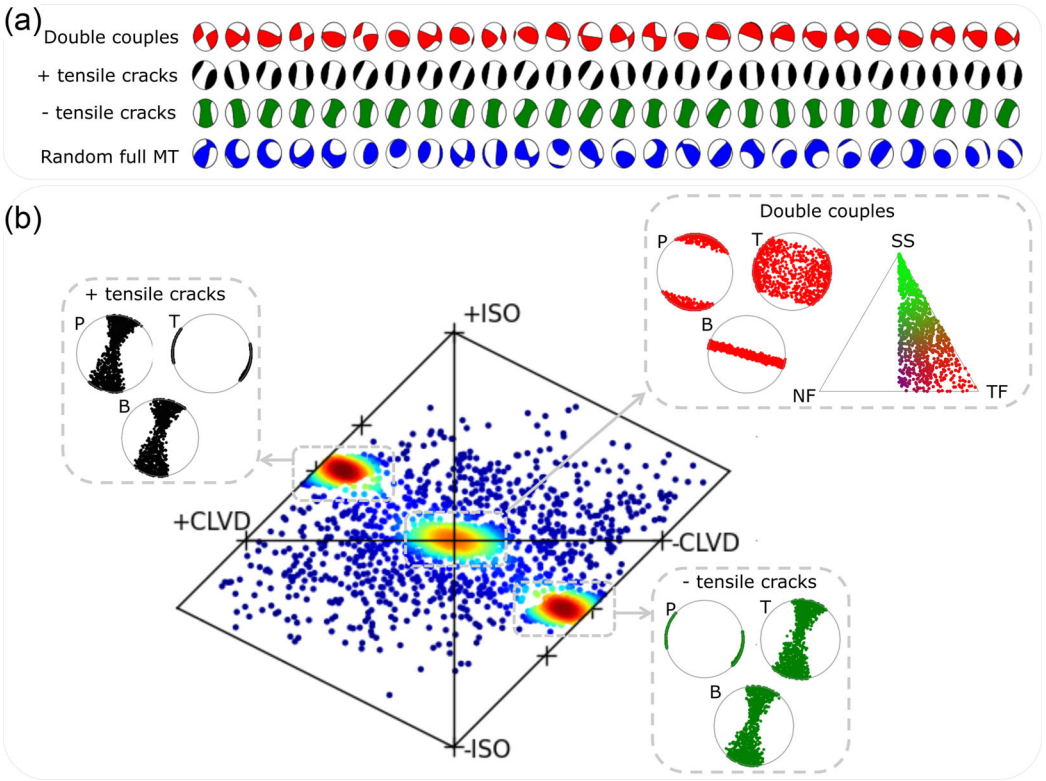

Figure 2. (a) Examples of focal mechanisms for different families of expected microseismicity in hydraulic fracturing. (b) Hudson source-type plot showing the Gaussian Kernel density for the complete synthetic microseismic catalogue, where red denotes higher and blue regions lower event densities, respectively. The boxes with dashed grey frames identify the concentrations of seismic sources and the *T*, *P* and *B* axes plots belonging to the double-couple, positive and negative tensile crack families. The triangle diagram indicates the distributions of double-couple focal mechanism. The blue points dispersion corresponds to the random full moment tensor family. Acronyms in Hudson plot mean isotropic (ISO) and compensated linear vector dipole (CLVD).

The last family (family 4), defined as 'random full moment tensor', represents random moment tensor sources and thus account unexpected processes. This family shows a clear dispersion both in the Hudson and focal mechanism orientation plots.

A proper representation of microseismicity should further consider a suitable distribution of magnitudes and hypocentres (Fig. 3). The instrumental sampling of our fracking experiment (500 Hz) and the distance to the horizontal fracking drillings (∼4 km depth) do not favour detections with moment magnitude below −1; on the other hand, the few previous hydraulic fracturing experiments in Europe never reported seismicity of magnitude greater than 3 (Clarke *et al*. 2014). We then adopt a Gutenberg–Richter distribution with $b = 1$ and $a = 1.84$, to distribute magnitudes in between these limits. Moreover, we assume a circular fault model of Madariaga (1976) and an average stress drop of 2.7 MPa for earthquakes within the chosen magnitude range (Kwiatek *et al*. 2011). Based on this, we can estimate a maximum rupture length of ∼350 m for the largest events. This value can be used to define the spatial distribution of induced seismicity, in coherence with previous results in the United States, where most of the maximum fracture lengths have been less than 100 m, reaching peak values of 600 m (e.g. Davies *et al*. 2012; Fisher & Warpinski 2012). We consider that the hypocentres of small fractures are constrained within a volume defined by the maximal possible rupture, which extends 350 m around the segments of the horizontal wells where the fracking takes place. This corresponds to a worst case scenario, where the largest fracture nucleates close to the well and propagates unilaterally for the length of 350 m. While the induced seismicity events (families 2 and 3) are constrained within this volume (Fig. 3a), background DC sources (family 1) and random sources (family 4) are randomly distributed in a slightly broader region (Fig. 3b). Origin times are distributed randomly within a time period of one month (which is in the order of the duration of the whole fracking process). As a result of this procedure we obtain a catalogue of 4000 synthetic events, divided in four families. The catalogue includes the following information: origin time, location, moment magnitude, moment tensor and its decomposition into isotropic, DC and compensated linear vector dipole, radius, duration, stress drop and event family.

After generating the synthetic seismic catalogue, we compute the respective seismograms at all the stations of the monitoring network, both at the surface and at the shallow borehole installations. A realistic local crustal model is necessary to properly compute the synthetic waveforms. A 1-D velocity profile could be modeled from ground samples of the vertical fracking drilling. Since we do not dispose of such information, we relied on previous studies on the broader region of interest. We use a *P*-wave velocity profile extracted from a high-resolution 3-D seismic model for Poland, at the location of the fracking site (Grad *et al*. 2015), which is shown in Fig. 4. The *S*-wave velocity profile was built assuming a typical scaling to the *P*-wave velocity ($v_p = 1.73\ v_s$), while densities of each layer were obtained from Grabowska *et al*. (1998). A constant attenuation factor is used for all layers ($Q_p = 120$ and $Q_s = 60$, Król *et al*. 2013). The low Q value for S and P waves is representative for the sedimentary basin in Poland and leads to a high attenuation in the frequency range of study. The reflectivity method (Wang 1999) was used to precalculate Green functions up to 500 Hz for the chosen velocity model and a proper range of source depths and epicentral distances. Finally, three-component

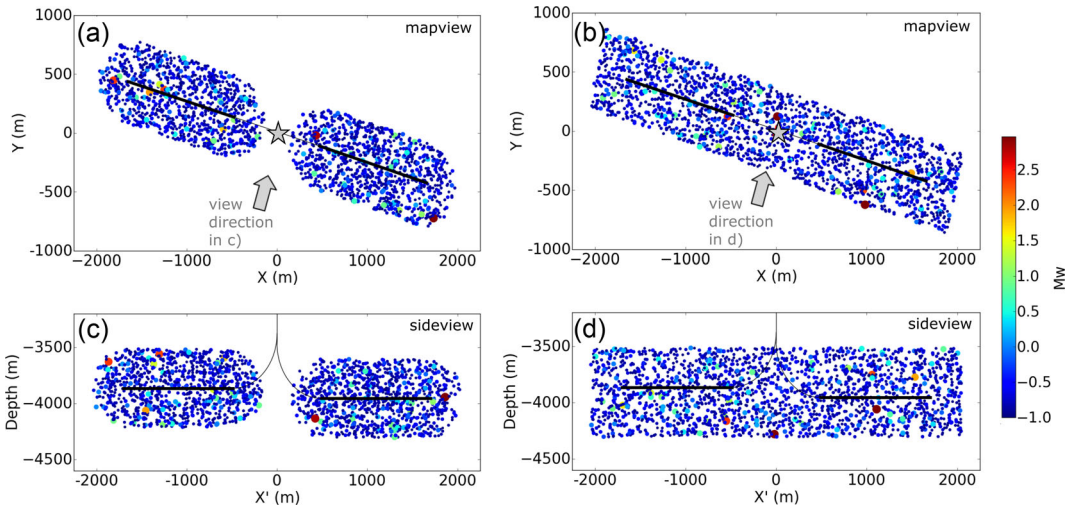

Figure 3. Distribution of hypocentres and magnitudes for the synthetic microseismic catalogue in the Wysin fracturing area. (a) Distribution for the random full moment tensor and double-couple families. (b) Distribution for the positive and negative tensile crack families. The size and colour of each point is scaled to the moment magnitude. Grey star indicates the vertical drilling. Black lines show the fracking boreholes and the thicker line identifies the zone allocated for fluid injection. Panels (a) and (b) show the map views, and (c) and (d) the side views.

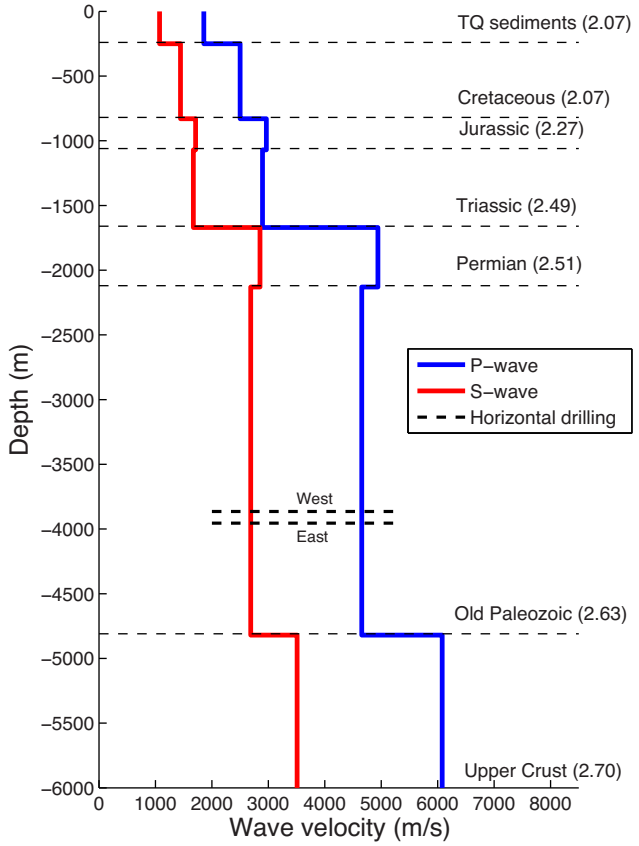

Figure 4. Local crustal model for the Wysin site. The *P*-wave velocity profile is obtained for the coordinates 54.09°N and 18.30°E from Grad *et al*. (2015). Each layer is identified with the name and the density value in g cm^{-3}. The thick black dashed lines indicate the depth of the west and east horizontal wells.

synthetic full waveforms (Fig. 5a) were generated using the Pyrocko package (http://emolch.github.io/pyrocko/, Heimann *et al*. 2014), combining the Green's functions and moment tensors of the synthetic catalogue. We convolve synthetic seismograms with the transfer functions of each receiver. Finally, to reproduce true monitoring conditions at the different station locations, we add real noise to synthetic traces (Fig. 5b), using recordings at those stations from 2016 May. Thereby, we can use different synthetic data sets: noise-free synthetic seismograms and noise contaminated continuous seismograms.

4 DETECTION PERFORMANCE USING AMPLITUDE THRESHOLD

Any detection algorithm needs to define a threshold or trigger level according to boundary conditions. Records of ambient noise during a time period prior to a seismic experiment are always useful in order to estimate suitable values for such detection level. As a prior approximation to assess the monitoring detection performance, we propose to compare the maximum amplitudes of our synthetic waveforms with an amplitude threshold previously defined according to the real noise records at each station. First, the maximum amplitudes of noise free synthetic full waveforms are analyzed in function of the hypocentral distance (r) and the moment magnitude (Fig. 6). The amplitude increases exponentially with the magnitude, while due to the geometrical spreading amplitudes decay with inverse dependence to the hypocentral distance ($1/r$). The variability of focal mechanisms and moment tensors in our catalogue is responsible for the amplitude variations with respect to this general patterns (see amplitude profiles in Fig. 6). In fact, we observe in general larger amplitudes associated with DC sources than tensile cracks. Second, a seismic noise analysis is carried out using one-month data (2016 May) before fracking operations to define the amplitude threshold.

The detection performance of each station will additionally depend on the specific noise conditions. Therefore, we consider random noise samplings at each station and used them to estimate an average noise conditions in terms of ground displacement (Fig. 7). Although the detection procedure would be actually performed on raw traces, our approach was chosen to quantify the detection amplitude in terms of maximal displacements. Choosing a physical magnitude such as displacement for the detection threshold is convenient for comparison with future studies, in order to be independent on the sensor instrumentation. Mean and standard

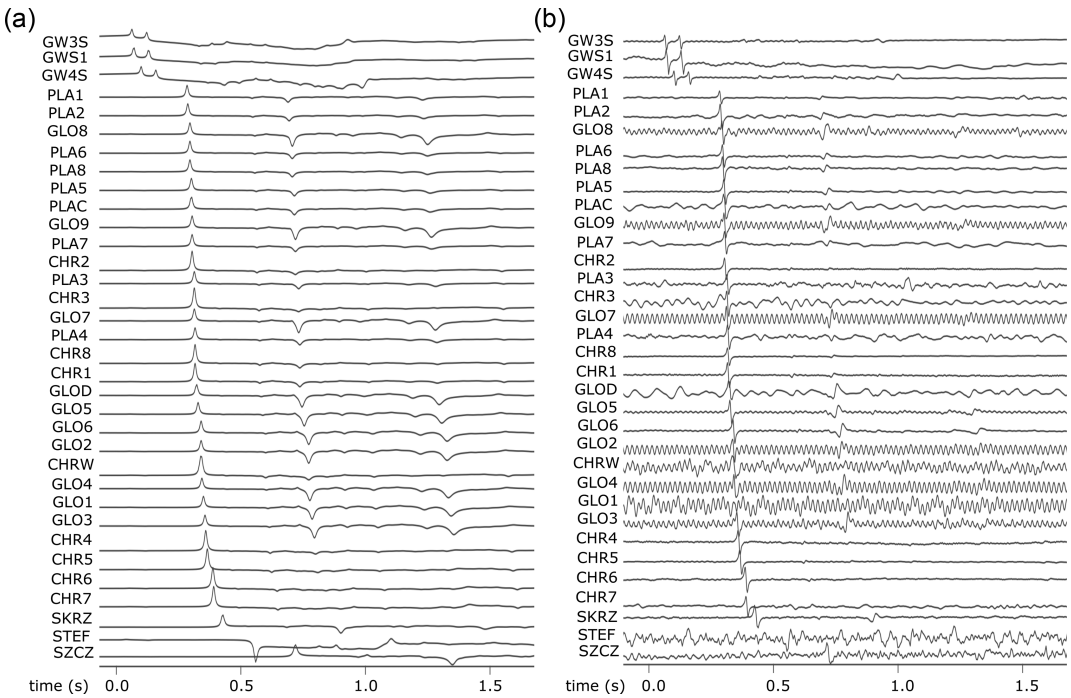

Figure 5. (a) Raw synthetic waveforms (displacement) and (b) real noise contaminated continuous seismograms (velocity) for one positive tensile crack event with $M_w = 0.97$. (a) and (b) show the same event for the vertical component in each seismic station. The signal in (b) is bandpass filtered between 2 and 80 Hz and notch filtered at 50 Hz. Zero time corresponds with the origin time.

deviation values are obtained from the noise sampling at different hours in order to observe daily variations. Larger noise levels during day hours (6.00–18:00 hr) are found as a general pattern. However, different patterns of smoother variations are also found for some stations (e.g. a noise level increase between 15:00 and 24:00 hr at CHR3 and GW4S, see Fig. 7a). We choose the amplitude threshold for each station according to the averaged values during the day and night hours (Fig. 7). In this way, we can clearly identify the most noisy stations between 2 and 80 Hz (e.g. PLA4, PLA7 and PLA8) and most quiet ones (e.g. GLO5 and GLO7). The borehole stations, which are located at shallow depth (around 50 m below surface) show similar noise levels between 2 and 80 Hz as some surface stations. The detector level is then defined according these amplitude thresholds and a fixed SNR.

We can now compare the maximal amplitude of noise-free synthetic waveforms at each station and the corresponding station noise level (either for day or night hour, depending on the event origin time). Imposing different SNR requirements, we can estimate detected and undetected events at each station. Thereby, the M_c can be calculated straight by the lowest magnitude above which all synthetic events are robustly detected (i.e. detected by at least four stations), taking into account both day and night amplitude thresholds (Fig. 8). The increase of M_c with required SNR reflects the fact that imposing a larger SNR for detection will decrease the number of detected events and increase the M_c. A potential empirical law can adjust this relation with fit parameters d_1 and d_2:

$$M_c = d_1 \mathrm{SNR}^{d_2} + d_0. \quad (1)$$

In this equation, since the noise level is fixed, a low SNR means that events which have low amplitude waveforms (i.e. small magnitude) can be detected; in the extreme case of SNR equal to 0, we should detect all synthetic events, so that d_0 can be defined by the minimum magnitude of our synthetic catalogue, in our case, $d_0 = -1$. The variation of M_c quantifies the monitoring performance of our network for different values of the SNR detection threshold. We estimate $M_c \sim 0.60$ during day hours and $M_c \sim 0.55$ during night hours, when considering a realistic SNR = 2. Another interesting issue concerns the evaluation of the contribution to M_c for each family of source mechanisms. The tensile crack families constrain the M_c for the complete synthetic catalogue, as these events are more difficult to be detected. Conversely, for the DC family alone, the M_c is reduced to ~0.1, for example, considering SNR larger than 1 (Fig. 8). The different detection performance arises from the fact that DC sources produce larger amplitudes than tensile cracks with the same magnitude, as previously discussed in Fig. 6. It should be noted, however, that this also implies some challenges in the correct estimation of the magnitude for both DC and tensile sources. An amplitude-based magnitude definition, ignoring the radiation pattern of different type of sources, may lead to underestimate the magnitude of tensile sources (or overestimate the magnitude of DC sources). Fit parameters in eq. (1) vary slightly for day, night and the selected family: d_1 [1.35–1.22]; d_2 [0.23–0.21]. Another important aim concerns the application of array techniques to improve the detection performance of our network. In general, the SNR improves with the square root of the number of stations belonging to an array (e.g. Rost & Thomas 2002, 2009). Applying such approximation to the three arrays, we can add fictitious stations located in the centre of each array (Fig. 1), with smaller amplitude thresholds. In this case, the fit parameter d_1 takes values between 1.29 and 1.17, and M_c is slightly decreased by about 0.05, with respect to the distributed network setup (Fig. 8).

Our next purpose aims to extend spatially the previous values of M_c around the fracking area for a realistic case of SNR = 2. We can obtain a map to assess our spatial performance combining the probability of detection (P_d) and empirical relations from Bayesian statistics. Taking into account each station and its corresponding amplitude threshold, we can divide the catalogue into detected (N^+) or not detected (N^-) events (Fig. 9a). The P_d at a single

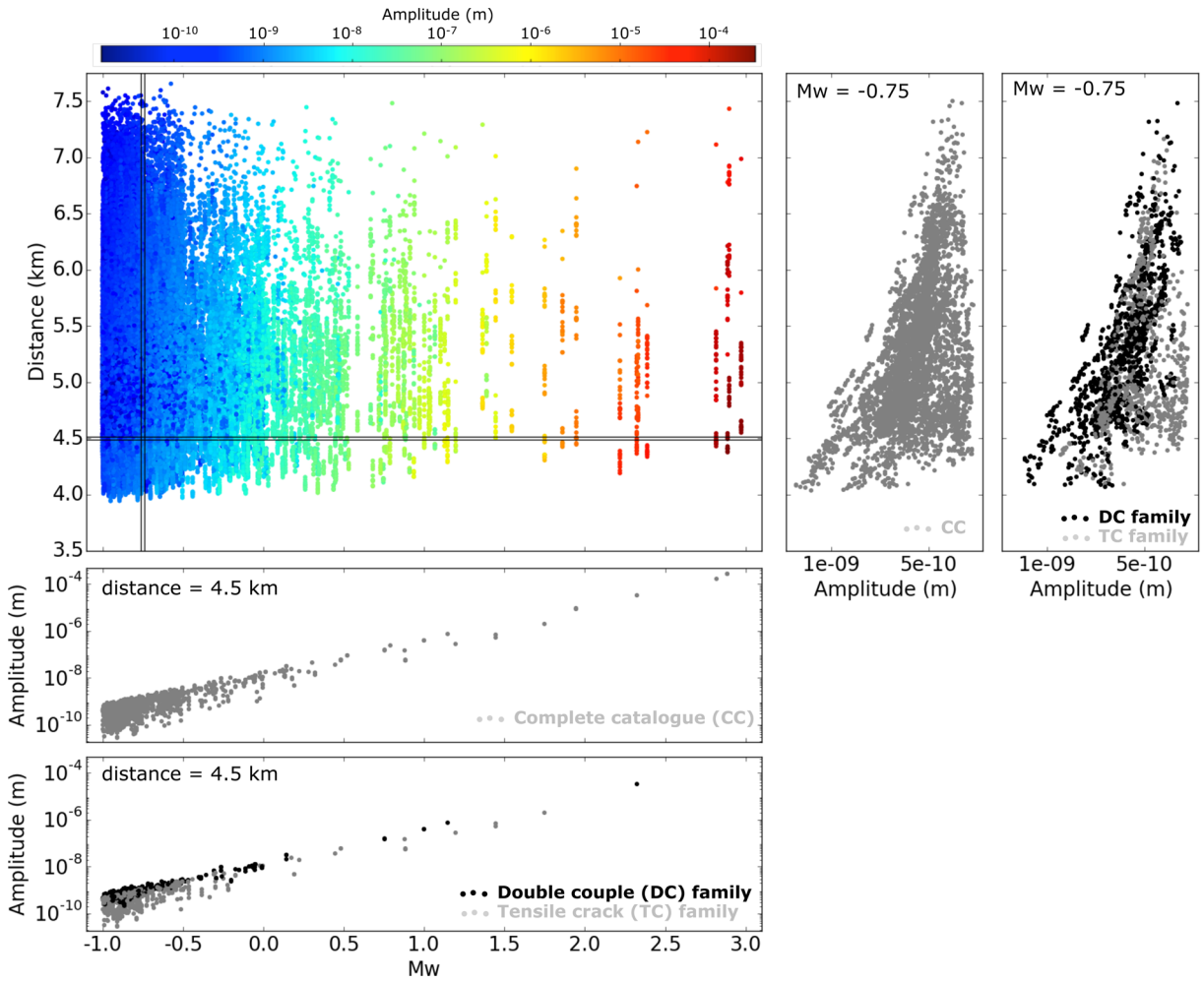

Figure 6. Maximum amplitudes according to the hypocentral distance for each station and the moment magnitude for each source are plotted for the complete synthetic microseismic catalogue. Amplitude profiles are plotted for a fixed hypocentral distance (4.5 km) and a fixed moment magnitude ($M_w = -0.75$) using grey dots. Additionally, we also show these same amplitude profiles considering those events belonging to the double-couple (black dots) and tensile crack (grey dots) families.

station for different magnitudes (M) and source–receiver distances (r) from the complete synthetic catalogue is estimated according to (Scholermmer & Woessner 2008):

$$P_d(M, r) = \frac{N_+}{N_+ + N_-}. \quad (2)$$

As a result, we obtain estimates of each single-station detection probability as a function of magnitude and hypocentral distance (Fig. 9a). However, this information is not complete for a broader domain of magnitudes and hypocentres, because of the limited spatial and magnitude distribution of the synthetic catalogue. In general, detection probabilities should not decrease with increasing magnitude or with decreasing source–receiver distance. The single-station detection performance can be extrapolate through empirical relationship such as in Mignan *et al.* (2011):

$$M_c(r, k) = C_1 r^{C_2} + C_3 \quad (3)$$

where M_c is dependent on the distance r to the kth nearest station with fit parameters C_1, C_2 and C_3. We scan the configurations of these coefficients, which are allowed to span within reasonable intervals (C_1 in [4, 12], C_2 in [0.04, 0.10] and C_3 in [−3, −10], Mignan *et al.* 2011; Mignan & Chouliaras 2014; Schultz *et al.* 2015b). These curves divide the magnitude–distance space in a region of large magnitude and small distances, where the detection is more likely, and a region of small magnitude and large distances, where the event detection is more difficult. The best configuration of C_1, C_2 and C_3 to define the completeness magnitude is here chosen only looking at the first region (below the curve) by (1) imposing that the number of detected events in this region by at least 95 per cent and (2) by maximizing the number of events in this region (Fig. 9). A shift is observed in this empirical relation towards larger magnitudes for the noisiest stations and, conversely, for quiet stations. The same analysis is performed for each array, which has the best detection performance (Fig. 9). A regular grid at an averaged depth for the horizontal fracking drillings of 3.91 km is fixed to map spatially the M_c, based on the previous empirical relations and imposing again the simultaneous detection by at least four stations (Fig. 10). Ignoring the noise heterogeneity on the surface, then the minimum values of the M_c would be found at the array locations, because of the larger station density. Considering real station-dependent noise conditions alter significant the spatial distribution of the detection performance, with a decrease in the M_c around the fracking area to match similar values such as those in Fig. 8.

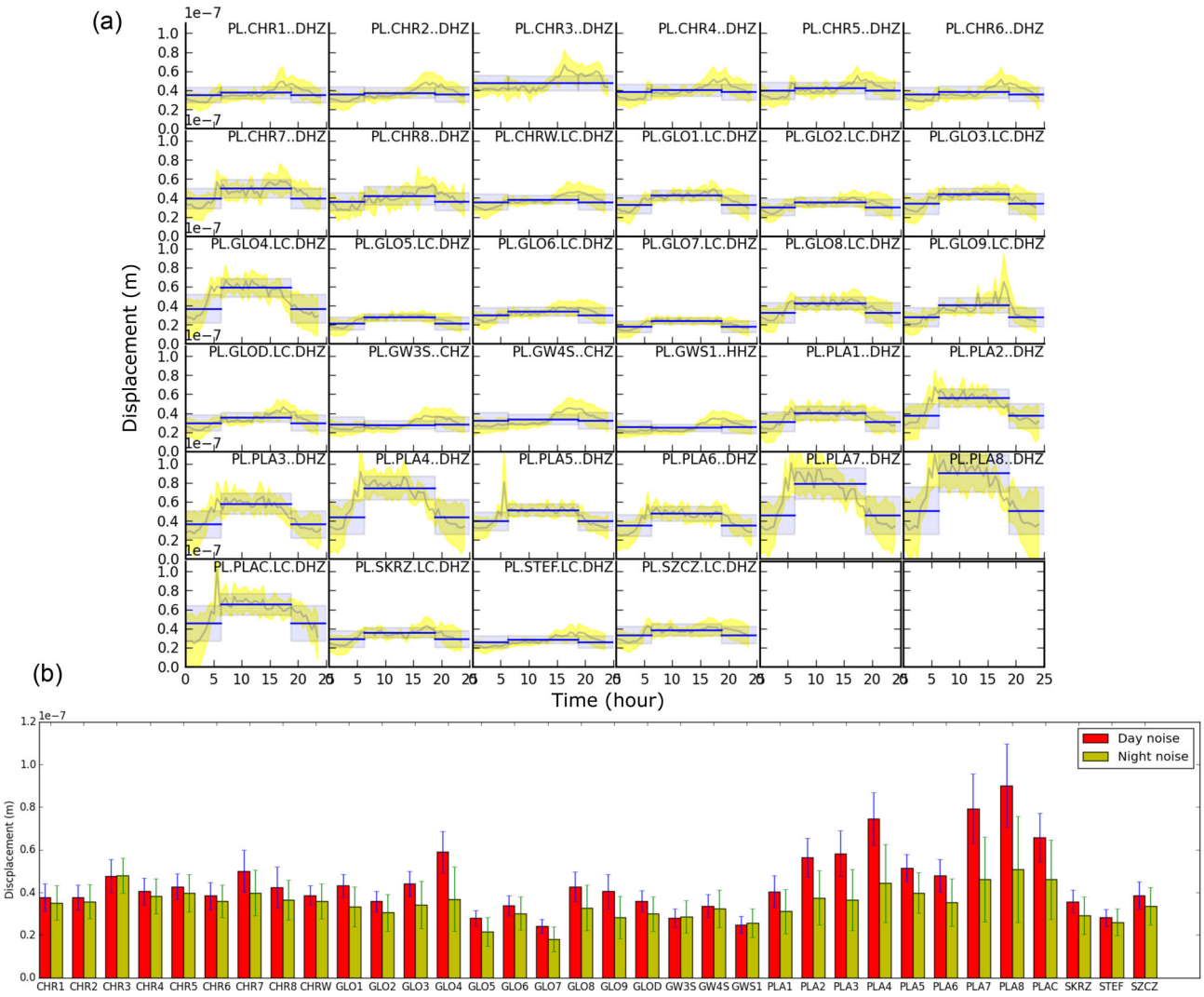

Figure 7. Noise analysis in each seismic station using one-month data between 2 and 80 Hz (vertical component) before fracking operations. (a) Mean (grey line) and standard deviation (yellow area) values in displacement are obtained from the random noise sampling taking into account the different hours of the day. Average amplitude threshold for day and night (blue line) and the standard deviation (light blue area) are estimated according the diurnal variation between 6:00 and 18:00 hr. (b) Bars diagram with the amplitude thresholds and its uncertainties during day (red bar) and night (yellow bar) for each station.

5 DETECTION PERFORMANCE USING COHERENCE

Automatic event detection and location procedures for monitoring local and regional seismicity are widely used by the seismological community. Coherence techniques have improved the traditional automatic detectors [e.g. short-term average (STA)/long-term average (LTA) techniques] and have been employed in microseismicity case for hydrofracking (López-Comino *et al*. 2017). Our next approach proposes to apply a recently developed automated full waveform detection and location algorithms (Lassie, https://gitext.gfz-potsdam.de/heimann/lassie, Matos *et al*. 2016; Heimann *et al*., in preparation), using real noise contaminated continuous seismograms. We simulate a continuous synthetic data set by convolving synthetic seismograms from the complete catalogue with the instrumental response and adding real noise, which is chosen randomly from the 2016 May data set but constrained around the average timing of the signal, so to preserve the daily variation of seismic noise. This python-tool earthquake detector is based on the stacking of characteristic functions of *P* and *S* waves according to the energy variations calculated from the square amplitudes of each trace. It follows a delay-and-stack approach, where the likelihood of the hypocentral location in a chosen seismogenic volume is mapped by assessing the coherence of arrival times at different stations (see Cesca & Grigoli 2015 for an overview). However, in the Lassie implementation, the adoption of smooth characteristic function calculated from normalized amplitude envelopes allows to reduce the spatial and temporal sampling (Heimann *et al*., in preparation). Data are first bandpass filtered between 2 and 80, Hz including an additional notch filter at 50 Hz (see Fig. 5b). The characteristic *P*- and *S*-wave functions for each station are then calculated, shifted and stacked according to *P* and *S* average velocities in our study region. These operations results in a spatiotemporal matrix of coherences values. The detection is performed searching the maximal spatial coherence at each time step, defining a detection every time this value trespasses a chosen threshold (Fig. 11).

The performance of this tool strongly depends on the selection of the coherence threshold. Consequently, we need to define an optimal detector level, able to detect weak events while not increasing excessively the number of false detections (Fig. 12). First tests

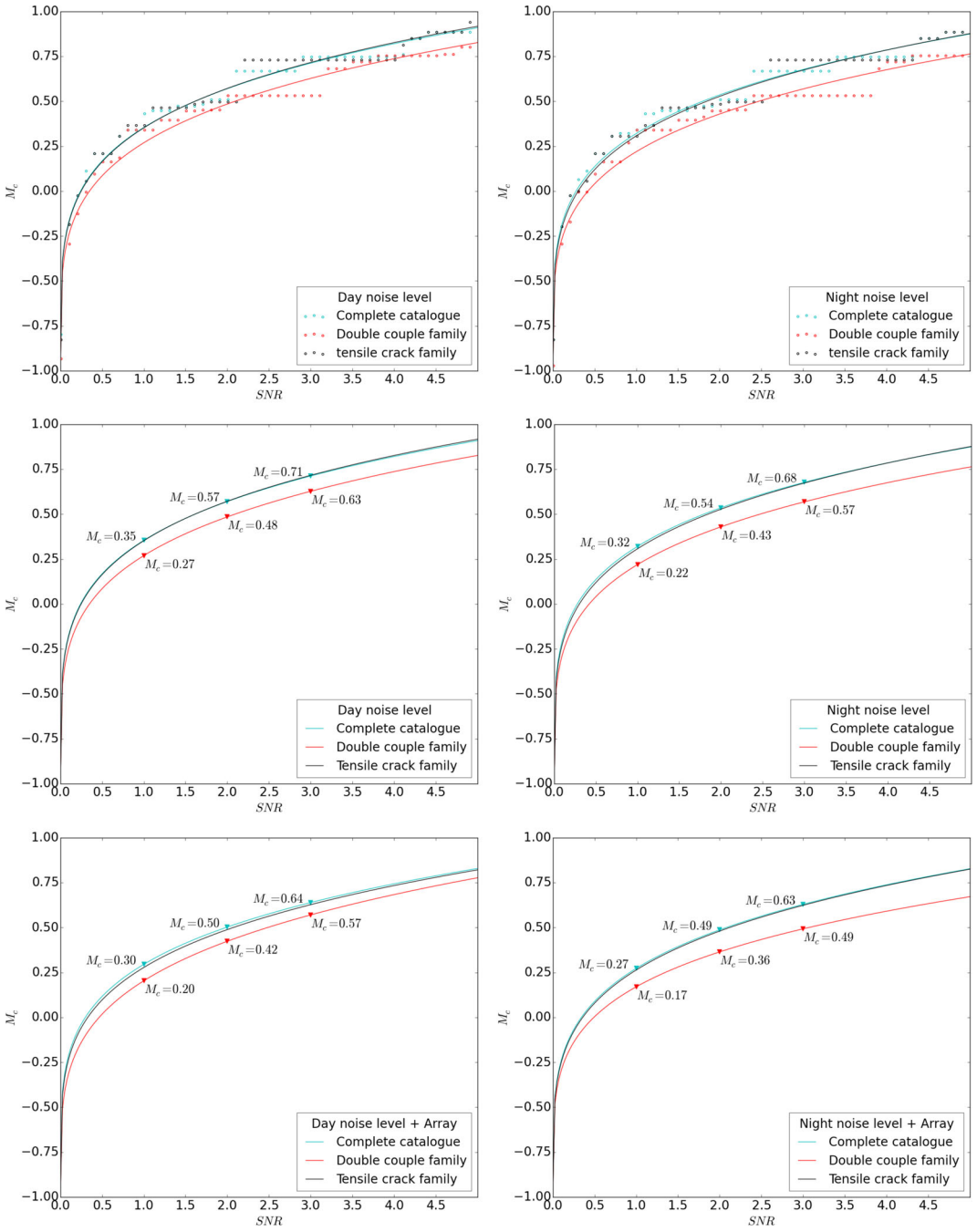

Figure 8. M_c versus SNR relation according to the noise levels during day (first column) and night hours (second column). Potential empirical laws can adjust the stepwise increase observed for our synthetic catalogue (first row). The monitoring performance is assessed for the Wysin network in terms of M_c for the SNR values of 1, 2 and 3 (second row). Note that we show the same empirical laws in first and second rows. The monitoring performance is improved using array techniques (third row). Cyan lines identify the curve using the complete synthetic catalogue, red lines those for the events included in the double-couple family and black lines those for the tensile crack family only.

indicate that events with M_w lower than -0.6 are entirely hidden in the real noise requiring too low detector levels, which would produce a great number of false detections. We show here the results using thresholds larger than 700 to remove these inconsistencies. A conservative choice would correspond to values able to minimize the number of false detections generated for random coherences in our data set. A better alternative is to require a threshold, for which the number of real detections is larger than the number of false detections. Our synthetic catalogue suggests appropriate thresholds could be chosen between 800 and 1000, with better performance during night hours, where the false detections disappear at threshold of ∼950. The detection performance depends on the chosen detector threshold in a similar way as in the previous case, using amplitude threshold with different SNR values (Figs 8 and 12). M_c shows again a stepwise increase with the detection threshold, but the monitoring performance is significantly improved thanks to the application of this waveform-based technique. If we consider a reasonable threshold (e.g. 950), where only 1 per cent of false detections are accepted, the M_c reaches values around 0.4 and 0.1 during day and night hours, respectively.

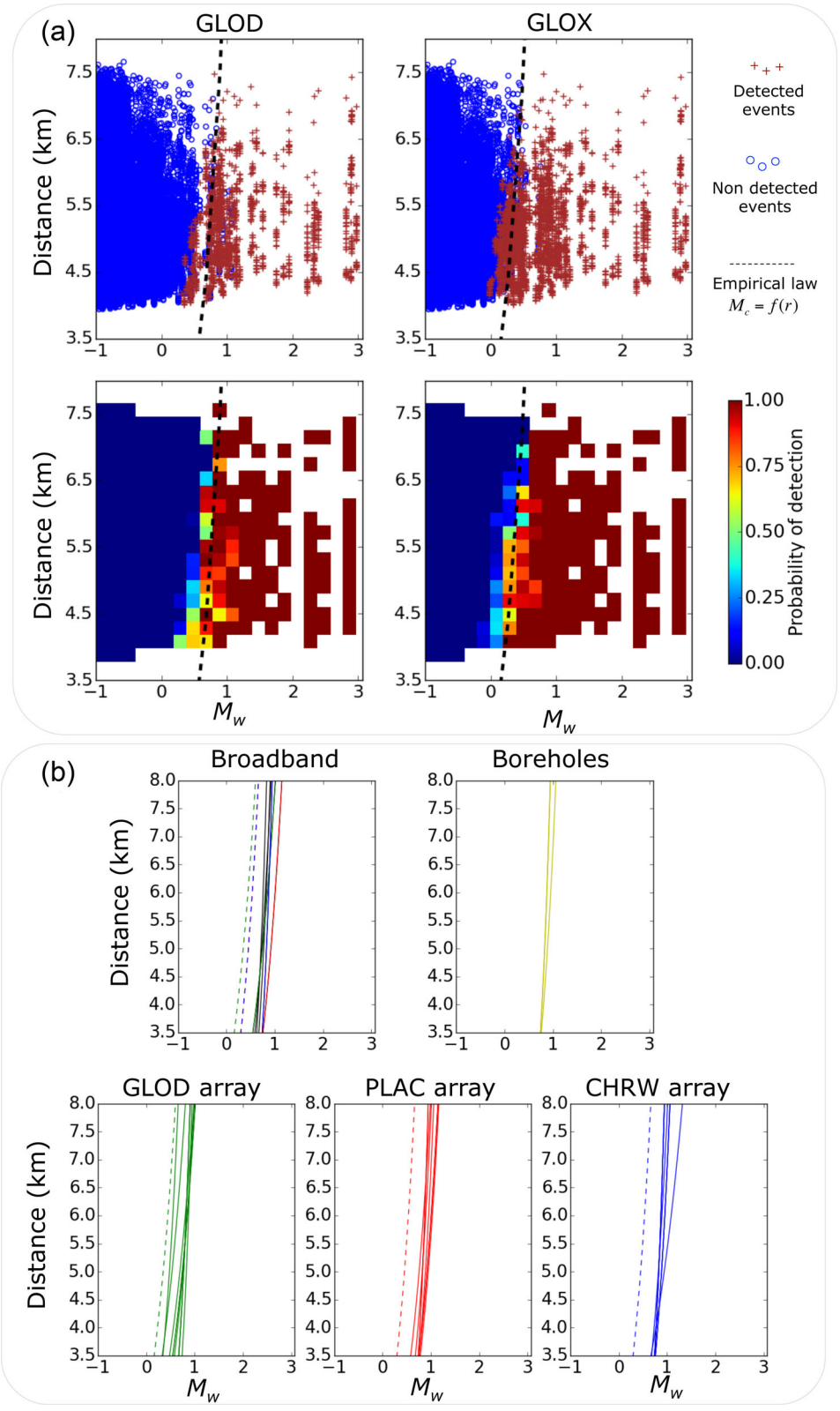

Figure 9. (a) Plot of all detected (brown crosses) and not detected events (blue circles) for the synthetic catalogue using an amplitude threshold previously calculated with real noise and SNR = 2 in the seismic station GLOD and the fictional stations for the array GLOX (first row). Probability of detections in the previous two stations (second row). Black dashed lines show the empirical relationship obtained by eq. (3). (b) Empirical relationship for all stations (solid lines) and fictional stations for the array (dashed lines). Stations in array GLOD are shown in green, array PLAC in red, array CHRW in blue and borehole stations in yellow. The inbox for the broad-band stations show in black colour the stations SZCZ, STEF and SKRZ; GLOD in green; PLAC in red and CHRW in blue.

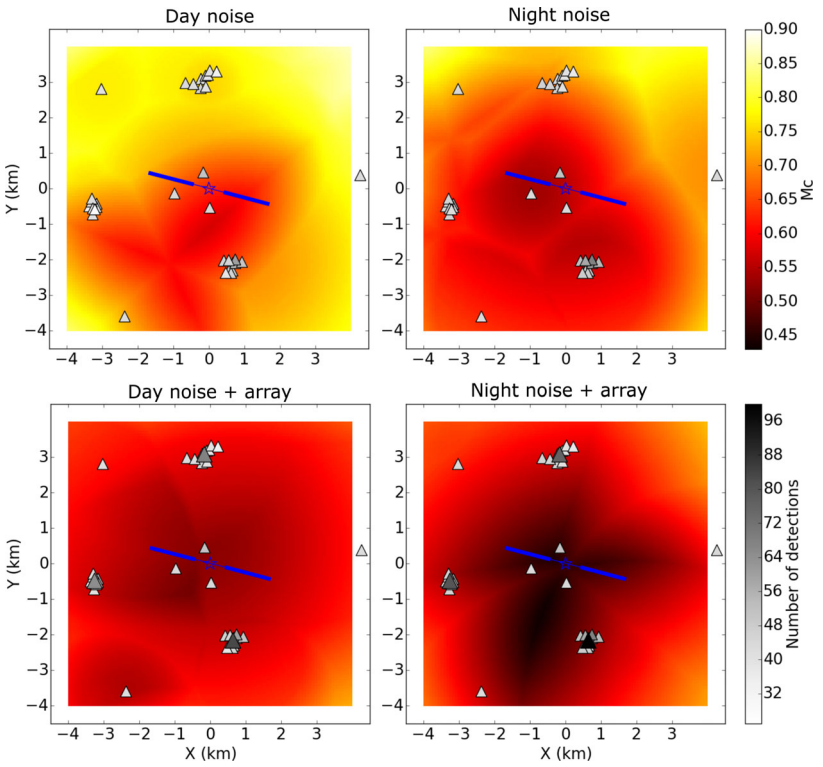

Figure 10. Spatial monitoring performance at Wysin site in terms of magnitude of completeness using an amplitude threshold estimated from real noise during day hours (first column) and during night hours (second columns) with SNR = 2 (first row). Improved spatial monitoring performance using array techniques (second row). Grey colour scale identifies the number of synthetic events detected for each station.

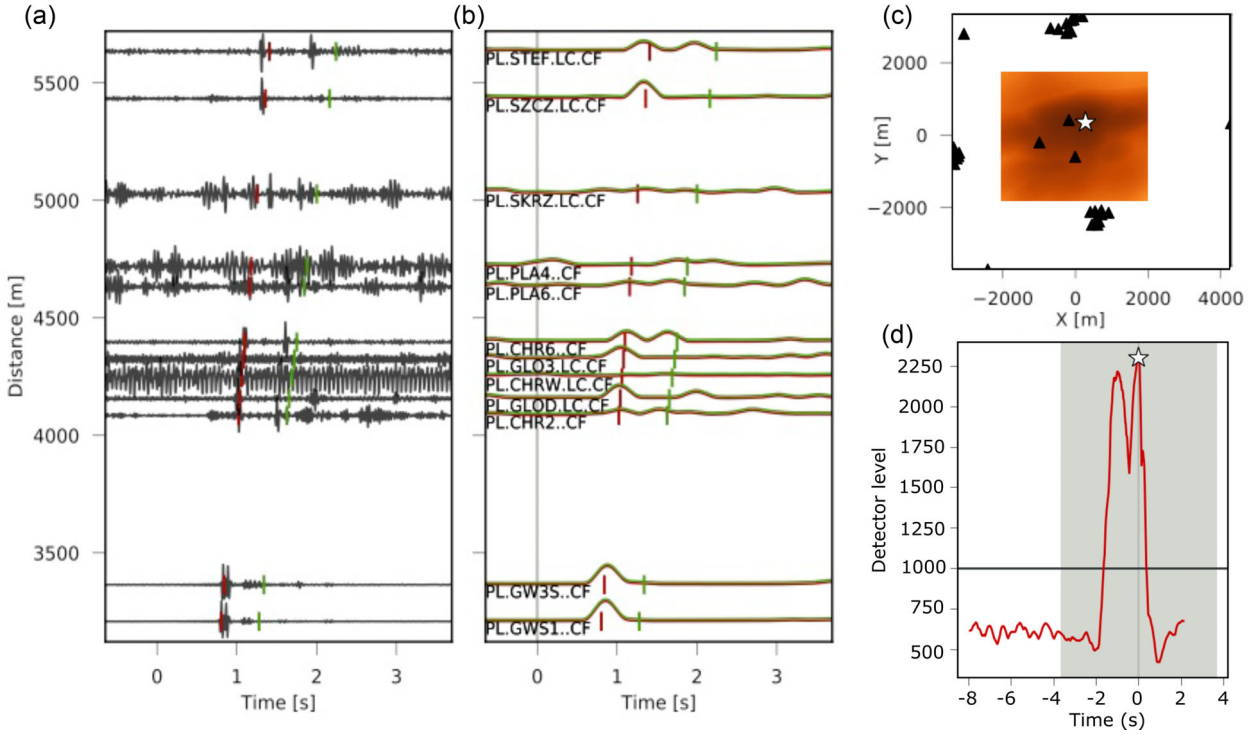

Figure 11. Example of synthetic event with $M_w = 0.8$. (a) Waveforms sorted by hypocentral distance for some example stations. (b) Characteristic function (normalized amplitude envelopes) for each trace. These are used for traveltime stacking corrected with *P*-wave speed (red lines) and *S*-wave speed (green lines). The markers indicate the (best-fit) synthetic arrival time of the respective phases at each sensor. (c) Coherence (stack) map for the search region. Dark colours denote high coherence values. A white star marks the location of the detected event. Sensor locations are shown with black triangles. (d) Global detector level function in a processing time window from −8 to +4 s around the origin time of the detected event. The cut-out time window used for the coherence map is shown in grey colour. White stars indicate this detection within the same processing time window, exceeding a detector level threshold of 1000.

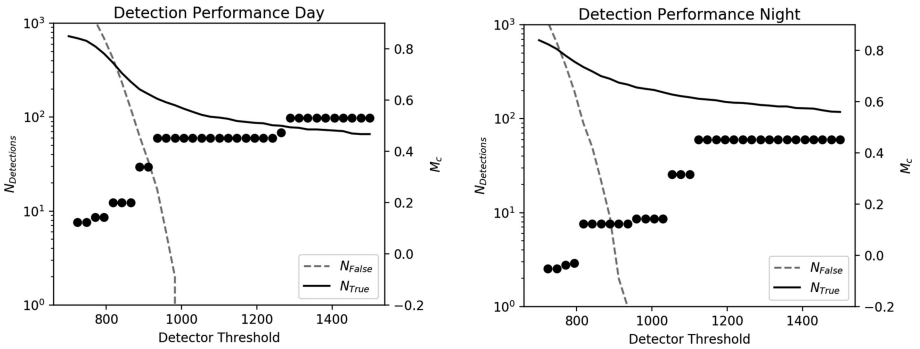

Figure 12. Detection performance using coherence techniques (Heimann *et al*., in preparation) for the synthetic catalogue with different detector thresholds. Continuous synthetic data set is generated adding real noise randomly distributed during day (left) and night (right) hours. The number of real detections corresponding with the synthetic catalogue (black line) and the number of false detections (grey dashed line) are shown. Black dots represent the values of magnitude of completeness for different detector threshold.

6 DISCUSSION AND CONCLUSIONS

The monitoring performance of a microseismic monitoring network is addressed through a robust parameter, such as M_c. However, this measure is usually estimated retroprospective, once we know the detected and located seismicity from a defined catalogue in a given region. In addition, the effects of changes in the number and type of instruments, as well as the available locations for installation, cannot be tested retroprospectively. Our approach aims to evaluate a prospective testing process that could generate induced seismicity taking as a starting point a seismic network previously designed and installed. The particular case of hydrofracking at the Wysin site is a good real example involving a combination of shallow and shallow depth monitoring. A realistic microseismic synthetic catalogue allows quantifying in terms of M_c our particular monitoring performance using noise recording before the fracking operations. Synthetic waveforms analysis could reveal important aspects about the seismicity we may record during and after fracking. Moreover, an adequate noise analysis is essential to know the current situation of our monitoring before the fracking operations starts.

An average amplitude threshold is estimated for each station from real noise recording reflecting diurnal variations that affects the detection performance. Although the lowest noise level are expected *a priori* in the shallow borehole stations, some surface stations are able to reach between 2 and 80 Hz similar or event better noise conditions. We used the raw synthetic seismogram to compare the maximum amplitudes of synthetic waveforms and average noise levels. The resolved detection performance can be adjusted by empirical relationships for different SNR values. This helps to extrapolate our estimations of completeness magnitude to a broader study region. We found that the detection performance is strongly varying for different day hours, with a better performance during quiet night hours. At the same time, M_c also differs for different source processes, so that tensile cracks are more difficult to detect than DC sources with the same magnitude. This may have important consequences when coming to the interpretation of detected seismicity, since the DC background seismicity may be better detected than induced seismicity. Assuming an SNR $= 2$, we estimate an $M_c \sim 0.55$ around the fracking area, with an increase of 0.05 during day hours. Combining the distributed network with the application of three small-scale arrays in about 3 km distance to the boreholes, M_c can be lowered to $\sim$0.45 at the fracking region.

The application of a novel automated detection algorithm, based on the detection of coherence signals at multiple stations, even in presence of noisy records, is able to improve substantially the detection performance. An essential requirement is to choose a reasonable detector level to avoid greater number of false detections and maximize the real detections at the same time. Again, these procedures are usually applied during and after the fracking operations. However, combining synthetic events and real noise, we have been able to create realistic noise contaminated continuous seismograms, which allow to define a suitable threshold for the detector and to quantify the expected M_c. We estimate for the Lassie detector (Heimann *et al*., in preparation) an efficient threshold around 950 for which 1 per cent of false detections are accepted. The M_c is improved using this methodology, so that we could detect all synthetic events with M_w larger than 0.1 during night hours.

This study proposes a valuable approach to combine synthetic catalogue, synthetic waveform generation and noise recordings during a pre-operational phase, to properly prepare detection tools and to estimate their performance, prior to the beginning of geomechanical operations which may trigger or induced seismicity. The generation of realisitc synthetic data requires an accurate investigation of source parameters and local structural models. If these conditions are met, the synthetic data can be a useful tool to assess the detection performance, but can also be used to assess the performance of further seismological analysis, for example, to judge the uncertainty on location procedures, or the evaluate the potential of modeling/inversion techniques for source parameter determination. The approach can be easily adapted to other environments implying the detection and characterization of induced microseismicity.

ACKNOWLEDGEMENTS

This work is funded by the EU H2020 SHale gas Exploration and Exploitation induced Risks (SHEER) project (www.sheerproject.eu—grant agreement no. 640896). The synthetic data for this paper are available by contacting the corresponding author at jalopez@gfz-potsdam.de.

REFERENCES

Amorese, D., 2007. Applying a change-point detection method on frequency- magnitude distributions, *Bull. seism. Soc. Am.*, **97,** 1742–1749.

Baig, A. & Urbancic, T., 2010. Microseismic moment tensors: a path to understanding frac growth, *Leading Edge,* **29,** 320–324.

Baranova, V., Mustaqeem, A. & Bell, S., 1999. A model for induced seismicity caused by hydrocarbon production in the Western Canada Sedimentary Basin, *Can. J. Earth Sci.,* **36**(1), 47–64.

British Columbia Oil and Gas Commission Report, 2012. Investigation of observed seismicity in the Horn River Basin, Available at: https://www.bcogc.ca/node/8046/download, last accessed 20 April 2017.

Cao, A.M. & Gao, S.S., 2002. Temporal variations of seismic *b*-values beneath northeastern Japan island arc, *Geophys. Res. Lett.,* **29,** 48-1–48-3.

Cesca, S. & Grigoli, F., 2015. Chapter two—full waveform seismological advances for microseismic monitoring, *Adv. Geophys.,* **56,** 169–228.

Cesca, S., Grigoli, F., Heimann, S., Gonzalez, A., Buforn, E., Maghsoudi, S., Blanch, E. & Dahm, T., 2014. The 2013 September–October seismic sequence offshore Spain: a case of seismicity triggered by gas injection?, *Geophys. J. Int.,* **198**(2), 941–953.

Clarke, H., Eisner, L., Styles, P. & Turner, P., 2014. Felt seismicity associated with shale gas hydraulic fracturing: the first documented example in Europe, *Geophys. Res. Lett.,* **41,** doi:10.1002/2014GL062047.

D'Alessandro, A., Luzio, D., D'Anna, G. & Mangano, G., 2011a. Seismic network evaluation through simulation: an application to the Italian National Seismic Network, *Bull. seism. Soc. Am.,* **101**(3), 1213–1232.

D'Alessandro, A., Papanastassiou, D. & Baskoutas, I., 2011b. Hellenic Unified Seismological Network: an evaluation of its performance through SNES method, *Geophys. J. Int.,* **185,** 1417–1430.

D'Alessandro, A. & Stickney, M., 2012. Montana seismic network performance: an evaluation through the SNES method, *Bull. seism. Soc. Am.,* **102**(1), 73–87.

Davies, R.J., Mathias, S.A., Moss, J., Hustof, S. & Newport, L., 2012. Hydraulic fractures: how far can they go?, *Mar. Petrol. Geol.,* **37,** 1–6.

Davies, R., Foulger, G.R., Bindley, A. & Styles, P., 2013. Induced seismicity and hydraulic fracturing for the recovery of hydrocarbons, *Mar. Petrol. Geol.,* **45,** 171–185.

Economides, M.J. & Nolte, K.G., 2003. *Reservoir Stimulation,* pp. 5.1–5.14, John Wiley.

Ellsworth, W.L., 2013. Injection-induced earthquakes, *Science,* **341**(6142), doi:10.1126/science.1225942.

Farahbod, A.M., Kao, H., Walker, D.M., Cassidy, J.F. & Calvert, A., 2015. Investigation of regional seismicity before and after hydraulic fracturing in the Horn River Basin, northeast British Columbia, *Can. J. Earth Sci.,* **52**(2), 112–122.

Fisher, M.K. & Warpinski, N.R., 2012. *Hydraulic-Fracture-Height Growth: Real Data*, Society of Petroleum Engineers, p. 145949.

Gaite, B., Ugalde, A., Villaseñor, A. & Blanch, E., 2016. Improving the location of induced earthquakes associated with an underground gas storage in the Gulf of Valencia (Spain), *Phys. Earth planet. Inter.,* **254,** 46–59.

Gomberg, J., 1991. Seismicity and detection/location threshold in the southern Great Basin seismic network, *J. geophys. Res.,* **96**(B10), 16 401–16 414.

Grabowska, T., Bojdys, G. & Dolnicki, J., 1998. Three-dimensional density model of the Earth's crust and the upper mantle for the area of Poland, *J. Geodyn.,* **25,** 5–24.

Grad, M., Polkowski, M. & Ostaficzuk, S.R., 2015. High-resolution 3D seismic model of the crustal and uppermost mantle structure in Poland, *Tectonophysics,* **666,** 188–210.

Healy, J., Rubey, W., Griggs, D. & Raleigh, C., 1968. The Denver earthquakes, *Science,* **161**(3848), 1301–1310.

Heidbach, O., Tingay, M., Barth, A., Reinecker, J., Kurfeß, D. & Müller, B., 2008. The World Stress Map database release 2008, doi:10.1594/GFZ.WSM.Rel2008.

Heimann, S., Simone, C., Kriegerowski, M. & Dahm, T., 2014. Synthetic seismogram web service and Python tools, in *EGU General Assembly 2014,* Vienna, Austria. Geophysical Research Abstracts, Vol. 16, EGU2014–10466.

Holland, A.A., 2013. Earthquakes triggered by hydraulic fracturing in south-central Oklahoma, *Bull. seism. Soc. Am.,* **103**(3), 1784–1792.

Horner, R.B., Barclay, J. & MacRae, J., 1994. Earthquakes and hydrocarbon production in the Fort St. John area of northeastern British Columbia, *Can. J. Explor. Geophys.,* **30**(1), 39–50.

Hudson, J.A., Pearce, R.G. & Rogers, R.M., 1989. Source type plot for inversion of the moment tensor, *J. geophys. Res.,* **94,** 765–774.

Keranen, K.M., Savage, H.M, Abers, G.A. & Cochran, E.S., 2013. Potentially induced earthquakes in Oklahoma, USA: links between wastewater injection and the 2011 M_w 5.7 earthquake sequence, *Geology,* **41,** 699–702.

Kraft, T., Mignan, A. & Giardini, D., 2013. Optimization of a large scale microseismic monitoring network in northern Switzerland, *Geophys. J. Int.,* **195,** 474–490.

Kriegerowski, M., Cesca, S., Krüger, F. & Dahm, T., 2015. Approaching moment tensor inversion and Q factor tomography of Western Bohemia earthquake swarms, in *IUGG General Assembly 2015*, Prague, Czech Republic, https://www.czech-in.org/cm/IUGG/CM.NET.WebUI/CM.NET.WEBUI.scpr/SCPRfunctiondetail.aspx?confID=05000000-0000-0000-0000-000000000053&sesID=05000000-0000-0000-0000-000000003029&absID=07000000-0000-0000-0000-000000023656, last accessed 20 April 2017.

Król, M., Cichostepski, K., Dec, J. & Pietsch, K., 2013. Application of inverse Q filtering for improvement of seismic resolution in the Zechstein formation (SW Poland), *Geol. Geophys. Environ.,* **39,** 33–44.

Kværna, T. & Ringdal, F., 1999. Seismic threshold monitoring for continuous assessment of global detection capability, *Bull. seism. Soc. Am.,* **89**(4), 946–959.

Kværna, T., Ringdahl, F., Schweitzer, J. & Taylor, L., 2002. Optimized seismic threshold monitoring – part 1: Regional processing, *Pure appl. Geophys.,* **159** (5), 969–987.

Kwiatek, G., Plenkers, K. & Dresen, G., 2011. Source parameters of picoseismicity recorded at Mponeng Deep Gold Mine, South Africa: implications for scaling relations, *Bull. seism. Soc. Am,* **101**(6), 2592–2608.

López-Comino, J.A., Cesca, S., Heimann, S., Grigoli, F., Milkereit, C., Dahm, T. & Zang, A., 2017. Characterization of hydraulic fractures growth during the Äspö Hard Rock Laboratory experiment (Sweden), *J. Rock Mech. Eng.,* in review.

Madariaga, R., 1976. Dynamics of an expanding circular fault, *Bull. seism. Soc. Am.,* **66,** 639–666.

Maghsoudi, S., Cesca, S., Hainzl, S., Kaiser, D., Becker, D. & Dahm, T., 2013. Improving the estimation of detection probability and magnitude of completeness in strongly heterogeneous media, an application to acoustic emission (AE), *Geophys. J. Int.,* **193**(3), 1556–1569.

Maghsoudi, S., Cesca, S., Hainzl, S., Dahm, T., Zöller, G. & Kaiser, D., 2015. Maximum magnitude of completeness in a salt mine, *Bull. seism. Soc. Am.,* **105**(3) 1491–1501.

Marsan, D., 2003. Triggering of seismicity at short timescales following California earthquakes, *J. geophys. Res.,* **108**(B5), 2266, doi:10.1029/2002JB001946.

Matos, C., Heimann, S., Grigoli, F., Cesca, S. & Custódio, S., 2016. Seismicity of a slow deforming environment: Alentejo, south Portugal, in *EGU General Assembly 2016,* Vienna, Austria. Geophysical Research Abstracts, Vol. 18, EGU2016-278.

McGarr, A., Simpson, D. & Seeber, L., 2002. 40 Case histories of induced and triggered seismicity, *Int. Geophys.,* **81A,** 647–661.

Mignan, A. & Woessner, J., 2012. Estimating the magnitude of completeness for earthquake catalogs, Community Online Resource for Statistical Seismicity Analysis, doi:10.5078/corssa-00180805.

Mignan, A. & Chouliaras, G., 2014. Fifty years of seismic network performance in Greece (1964–2013): spatiotemporal evolution of the completeness magnitude, *Seismol. Res. Lett.,* **85**(3), 657–667.

Mignan, A., Werner, M.J., Wiemer, S., Chen, C.C. & Wu, Y.M., 2011. Bayesian estimation of the spatially varying completeness magnitude of earthquake catalogs, *Bull. seism. Soc. Am.,* **101**(3), 1371–1385.

Nanjo, K., Schorlemmer, D., Woessner, J., Wiemer, S. & Giardini, D., 2010. Earthquake detection capability of the Swiss Seismic Network, *Geophys. J. Int.,* **181**(3), 1713–1724.

Nicholson, C. & Wesson, R.L., 1990. Earthquake hazard associated with deep well injection: a report to the U.S. Environmental Protection Agency, *U.S. Geol. Surv. Bull.,* **1951,** 74.

Nicholson, C. & Wesson, R., 1992. Triggered earthquakes and deep well activities, *Pure appl. Geophys.,* **139**(3), 561–578.

Nolen-Hoeksema, R. & Ruff, L., 2001. Moment tensor inversion of microseisms from the B-sand propped hydrofracture, M-site, Colorado, *Tectonophysics,* **336,** 163–181.

Plenkers, K., Schorlemmer, D. & Kwiatek, G., 2011. On the probability of detecting picoseismicity, *Bull. seism. Soc. Am.,* **101**(6), 2579–2591.

Rydelek, P.A. & Sacks, I.S., 1989. Testing the completeness of earthquake catalogues and the hypothesis of self-similarity, *Nature,* **337**(6204), 251–253.

Rost, S. & Thomas, C., 2002. Array seismology: methods and applications, *Rev. Geophys.,* **40**(3), 1008, doi:10.1029/2000RG000100.

Rost, S. & Thomas, C., 2009. Improving seismic resolution through seismic arrays, *Surv. Geophys.,* **30,** 271–299.

Schorlemmer, D. & Woessner, J., 2008. Probability of detecting an earthquake, *Bull. seism. Soc. Am.,* **98**(5), 2103–2117.

Schultz, R., Stern, V. & Gu, Y.J., 2014. An investigation of seismicity clustered near the Cordel Field, west central Alberta, and its relation to a nearby disposal well, *J. geophys. Res.,* **119**(4), 3410–3423.

Schultz, R., Stern, V., Novakovic, M., Atkinson, G. & Gu, Y.J., 2015a. Hydraulic fracturing and the Crooked Lake Sequences: insights gleaned from regional, *Earth,* **36**(1), 47–64.

Schultz, R., Stern, V., Gu, Y.J. & Eaton, D., 2015b. Detection threshold and location resolution of the Alberta Geological Survey earthquake catalogue, *Seismol. Res. Lett.,* **86**(2A), 385–397.

Sereno, T. & Bratt, S.R., 1989. Seismic detection capability at NORESS and implications for the detection threshold of a hypothetical network in the Soviet Union, *J. geophys. Res.,* **94**(B8), 10 397–10 414.

Wang, R., 1999. A simple orthonormalization method for the stable and efficient computation of Green's functions, *Bull. seism. Soc. Am.,* **89,** 733–741.

Wiemer, S. & Wyss, M., 2000. Minimum magnitude of completeness in earthquake catalogs: examples from Alaska, the Western United States, and Japan, *Bull. seism. Soc. Am.,* **90**(4), 859–869.

Woessner, J. & Wiemer, S., 2005. Assessing the quality of earthquake catalogues: estimating the magnitude of completeness and its uncertainty, *Bull. seism. Soc. Am.,* **95**(2), 684–698.

Zang, A. & Stephansson, O., 2010. *Stress field of the Earth's Crust,* Springer, p. 322.